A method to derive Fourier-wavelet spectra for the characterization of global-scale waves in the mesosphere and lower thermosphere, and its Matlab and Python software (fourierwavelet v1.1)

Yosuke Yamazaki

Leibniz Institute of Atmospheric Physics at the University of Rostock

Schlossstraße 6, 18225 Kühlungsborn

Correspondence: Y. Yamazaki (yamazaki@iap-kborn.de)

Abstract. This paper describes a simple method for characterizing global-scale waves in the mesosphere and lower thermosphere (MLT), such as tides and traveling planetary waves, using two-dimensional longitude-time data. The technique involves two steps. In the first step, the Fourier transform is performed in space (longitude), and time series of the space Fourier coefficients are derived. In the second step, the wavelet transform is performed on these time series, and wavelet coefficients are derived. A 'Fourier-wavelet' spectrum can be obtained from these wavelet coefficients, which gives the amplitude and phase of the wave as a function of time and wave period. It can be used to identify wave activity that is localized in time, similar to a wavelet spectrum, but the Fourier-wavelet spectrum can be obtained separately for eastward- and westward-propagating components and for different zonal wavenumbers. The Fourier-wavelet analysis can be easily implemented using existing Fourier and wavelet software. Matlab and Python scripts are created and made available at [https://igit.iap-kborn.de/yamazaki/fourierwavelet] that compute Fourier-wavelet spectra using the wavelet software provided by Torrence and Compo (1998). Some application examples are presented using MLT data from atmospheric models.

1 Introduction

1.1 Background and motivation

The Earth's atmosphere can support various types of global-scale waves, which zonally extend around a full circle of latitude. Zonal wavenumber is defined as the number of wave cycles that fit within the latitude circle. As the wave propagates eastward or westward, an oscillation is observed at ground stations. The period of the oscillation depends on the zonal phase velocity and zonal wavenumber of the wave,

$$T = \omega^{-1} = \frac{2\pi R_E}{kC} \cos\phi, \tag{1}$$

where T (in s) is the wave period, ω (in s^{-1}) is the wave frequency, R_E (in m) is the Earth's radius, k is the zonal wavenumber, C (in m s^{-1}) is the phase speed, and ϕ (in rad) is the latitude.

Examples of global-scale waves in the atmosphere include atmospheric tides (Lindzen and Chapman, 1969; Forbes, 1984) and traveling planetary waves (Salby, 1984; Madden, 2007). Solar tides, with primary periods at 24 h and 12 h (called 'diurnal'

and 'semidiurnal' tides, respectively), are thermally excited through periodic absorption of solar radiation mainly in the troposphere and stratosphere (Forbes, 1982a, b). Dominant modes are the westward-propagating migrating (or Sun-synchronous) diurnal tide with zonal wavenumber 1 (DW1) and migrating semidiurnal tide with zonal wavenumber 2 (SW2). Besides, non-migrating (or non-Sun-synchronous) modes are also commonly observed, such as eastward-propagating diurnal tides with zonal wavenumber 3 (DE3) and 2 (DE2) (e.g., Hagan and Forbes, 2002; Forbes et al., 2008; Oberheide et al., 2011). Tides propagate vertically upward from the source region. Their amplitude increases with height due to the reduction of atmospheric density, until dissipation eventually takes place in the mesosphere and lower thermosphere (MLT) and prevents their further growth. As a result, the wave amplitude is often largest in the MLT region.

Traveling planetary waves have a period longer than a day and shorter than several weeks. Some are interpreted as Rossby normal modes, which are predicted by classical linear wave theory (e.g., Longuet-Higgins, 1968; Kasahara, 1976). Rossby normal modes are solutions to Laplace's tidal equation in an idealized atmosphere with no dissipation and mean winds, and represent free (or resonant) oscillations of the atmosphere (Forbes et al., 1995b). The behavior of traveling planetary waves in the real atmosphere deviates from what is anticipated from the linear wave theory due to dissipation and mean winds. Also, some traveling planetary waves in the MLT are considered to be unstable modes locally generated by atmospheric instability, rather than normal modes (e.g., Pfister, 1985; Meyer and Forbes, 1997). Traveling planetary waves that are most commonly observed in the MLT region have periods about 5–7 days (Hirota and Hirooka, 1984; Wu et al., 1994; Forbes and Zhang, 2017; Qin et al., 2021b), 9–11 days (Hirooka and Hirota, 1985; Forbes and Zhang, 2015) and 14–16 days (Forbes et al., 1995a; Day et al., 2011). They are all westward-propagating with zonal wavenumber 1, and called quasi-6-day wave (Q6DW), quasi-10-day wave (Q10DW) and quasi-16-day wave (Q16DW), respectively. Also in this category are the westward-propagating quasi-28-day wave (Q28DW) with zonal wavenumber 1 (Zhao et al., 2019), the westward-propagating quasi-4-day wave (Q4DW) with zonal wavenumber 2 (Ma et al., 2020; Yamazaki et al., 2021) and the westward-propagating quasi-7-day wave (Q7DW) with zonal wavenumber 2 (Pogoreltsev et al., 2002). The westward-propagating quasi-2-day wave (Q2DW) with zonal wavenumber 2–4 is also frequently observed in the MLT region (Wu et al., 1993; Gu et al., 2013; Moudden and Forbes, 2014; He et al., 2021), and is sometimes regarded as manifestation of mixed Rossby-gravity modes (e.g., Salby, 1981a; Salby and Callaghan, 2001). Although theoretical Rossby normal modes and mixed Rossby-gravity modes are westward-propagating, observations sometimes show eastward propagating components around the same period range (e.g., Palo et al., 2007; McDonald et al., 2011; Pancheva et al., 2018; Huang et al., 2021; Fan et al., 2022; Luo et al., 2023). Equatorial Kelvin waves (Matsuno, 1966; Holton and Lindzen, 1968) are equatorially-trapped eastward-propagating waves. At MLT heights, the ultra-fast Kelvin wave (UFKW) with zonal wavenumber 1 and a period of $\sim$3 days is frequently detected (e.g., Lieberman and Riggin, 1997; Forbes et al., 2009; Davis et al., 2012; Gasperini et al., 2015; Yamazaki et al., 2020b).

Neither tides nor traveling planetary waves are stationary. Generally, their amplitude varies with season. Besides, tidal amplitude shows marked day-to-day variability in the MLT region (e.g., Miyoshi and Fujiwara, 2003; Pedatella et al., 2012a; Wang et al., 2021b). This can be attributed to the interaction of tidal waves with the mean flow and other waves (e.g., Chang et al., 2011; Lieberman et al., 2015; Siddiqui et al., 2022) as well as to changes in the source of tides (e.g., Miyoshi, 2006; Siddiqui et al., 2019). Traveling planetary waves in the MLT region sometimes show a burst of wave activity that lasts for

a few wave cycles. This can be attributed to changes in the zonal mean state of the atmosphere, which controls propagation conditions, atmospheric instability, and critical layers (e.g., Salby, 1981b, c; Liu et al., 2004; Yue et al., 2012; Gan et al., 2018).

60   Tides and traveling planetary waves can be influenced by a sudden stratospheric warming, in which the mean state of the stratosphere and mesosphere is considerably altered. A sudden stratospheric warming is a large-scale meteorological disturbance, which usually takes place in the winter polar stratosphere (e.g., Butler et al., 2015; Baldwin et al., 2021). It can affect the whole atmosphere including different latitudes and height regions (e.g., Pedatella et al., 2018; Goncharenko et al., 2021). Enhanced tidal variability occurs in the MLT region during sudden stratospheric warming events (e.g, Fuller-Rowell et al., 2010;

65   Pedatella et al., 2012b; Jin et al., 2012; Siddiqui et al., 2018; Stober et al., 2020). Large amplification of traveling planetary waves is sometimes observed following sudden stratospheric warming events (e.g., Matthias et al., 2012; Sassi et al., 2012; Chandran et al., 2013; Gu et al., 2016; Yamazaki and Matthias, 2019; He et al., 2020; Wang et al., 2021a).

Understanding wave activity in the MLT region is important because it has a significant impact on the region above, i.e., the ionosphere and thermosphere (IT) (e.g., Liu, 2016; Yiğit and Medvedev, 2015). The IT region is where many space infras-

70   tructures operate, and is important for the radio communication between the ground and satellites (Schunk and Sojka, 1996; Moldwin, 2022). Many studies have found wave-like signatures in the IT region that correlate with tidal and traveling planetary wave activity in the MLT region (e.g., Laštovička, 2006; Immel et al., 2006; Oberheide et al., 2009; Pancheva and Mukhtarov, 2010; Gu et al., 2014; Yamazaki, 2018; Gan et al., 2020; Sobhkhiz-Miandehi et al., 2022). This is the motivation behind the present study, which introduces a simple spectral analysis method to evaluate global-scale wave activity in the MLT region.

75   The main objective of this study is to describe an easy-to-implement method to derive 'wavelet-like' spectra using longitude-time data. The wavelet analysis is a multiresolution analysis technique, which is widely used in research fields including the Earth science (e.g., Kumar and Foufoula-Georgiou, 1997; Torrence and Compo, 1998). A wavelet transform can be performed on one-dimensional (1-D) time-series data to derive a 'wavelet spectrum', which is usually presented in a time versus period diagram. The wavelet analysis is useful for identifying wave activity that is localized in time. This feature would also be useful

80   for studying global-scale waves in the MLT region, whose amplitude and phase are variable. However, the standard 1-D wavelet technique is not directly applicable to two-dimensional (2-D) longitude-time data, which are required for the characterization of global-scale waves. For spectral analysis of 2-D longitude-time data, Hayashi (1971) described a Fourier-based technique. In this study, Hayashi's method is combined with the wavelet technique so that it can detect global-scale wave activity that is localized in time.

85   ## 1.2 Fourier-based analysis of space-time data

Hayashi (1971) proposed a Fourier-based spectral analysis method for 2-D longitude-time data, which was successfully implemented in later studies (e.g., Mechoso and Hartmann, 1982; Wheeler and Kiladis, 1999; Miyoshi and Fujiwara, 2006; Akmaev et al., 2008; Sassi et al., 2016). The technique involves two steps. In the first step, the Fourier transform is performed in space (longitude), and time series of the sine and cosine Fourier coefficients are derived. In the second step, the Fourier transform is

90   performed on these time series. Hayashi (1971) clarified how the amplitude and phase of eastward- and westward-propagating

waves are related to the Fourier coefficients obtained from the second Fourier transform. What follows is a brief review of the technique of Hayashi (1971).

Assuming that perturbations of an atmospheric variable W (denoted by δW) at a fixed latitude can be expressed as the sum of eastward- and westward-propagating components with various zonal wavenumbers k (= 0, 1, 2, ...) and frequencies ω (>0; = ω_0, ω_1, ω_2, ...):

$$\delta W = \sum_k \delta W_k = \sum_k \left(\delta W_k^+ + \delta W_k^- \right), \tag{2}$$

where

$$\delta W_k^+ = \sum_\omega R_{k,\omega}^+ \cos \left(\omega t - k\lambda - \varphi_{k,\omega}^+ \right) \tag{3}$$

represents eastward-propagating components, and

$$\delta W_k^- = \sum_\omega R_{k,\omega}^- \cos \left(\omega t + k\lambda - \varphi_{k,\omega}^- \right) \tag{4}$$

is the westward-propagating counterpart. t and λ are time (in s) and longitude (in rad), respectively. R and φ are the amplitude and phase of the wave component, respectively, with the superscripts $+$ and $-$ indicating the eastward- and westward-propagating components, respectively. The above equations can be rearranged, and the component with zonal wavenumber k can be written as

$$\delta W_k = C_k(t) \cos kx + S_k(t) \sin kx, \tag{5}$$

with

$$C_k(t) = \sum_\omega \left(A_{k,\omega} \cos \omega t + B_{k,\omega} \sin \omega t \right) \tag{6}$$

$$S_k(t) = \sum_\omega \left(a_{k,\omega} \cos \omega t + b_{k,\omega} \sin \omega t \right), \tag{7}$$

where

$$A_{k,\omega} = R_{k,\omega}^+ \cos \varphi_{k,\omega}^+ + R_{k,\omega}^- \cos \varphi_{k,\omega}^- \tag{8}$$

$$B_{k,\omega} = R_{k,\omega}^+ \sin \varphi_{k,\omega}^+ + R_{k,\omega}^- \sin \varphi_{k,\omega}^- \tag{9}$$

$$a_{k,\omega} = -R_{k,\omega}^+ \sin \varphi_{k,\omega}^+ + R_{k,\omega}^- \sin \varphi_{k,\omega}^- \tag{10}$$

$$b_{k,\omega} = R_{k,\omega}^+ \cos \varphi_{k,\omega}^+ - R_{k,\omega}^- \cos \varphi_{k,\omega}^-. \tag{11}$$

Equations (8)–(11) can be further rearranged as follows:

$$R_{k,\omega}^\pm \cos \varphi_{k,\omega}^\pm = \frac{1}{2} \left(A_{k,\omega} \pm b_{k,\omega} \right) \tag{12}$$

$$R_{k,\omega}^\pm \sin \varphi_{k,\omega}^\pm = \frac{1}{2} \left(B_{k,\omega} \mp a_{k,\omega} \right), \tag{13}$$

from which R and φ can be derived as:

$$R_{k,\omega}^{\pm} = \frac{1}{2}\sqrt{\left(A_{k,\omega} \pm b_{k,\omega}\right)^2 + \left(B_{k,\omega} \mp a_{k,\omega}\right)^2} \tag{14}$$

$$\varphi_{k,\omega}^{\pm} = \arctan\frac{B_{k,\omega} \mp a_{k,\omega}}{A_{k,\omega} \pm b_{k,\omega}} \tag{15}$$

$R_{k,\omega}^{\pm}$ and $\varphi_{k,\omega}^{\pm}$ can be determined using longitude-time data sampled at a fixed latitude by, first, performing the Fourier transform in longitude to obtain time series of the sine and cosine Fourier coefficients (i.e., $S_k(t)$ and $C_k(t)$) and, then, performing the Fourier transform on $S_k(t)$ and $C_k(t)$ to obtain the sine and cosine Fourier coefficients (i.e., $B_{k,\omega}$, $b_{k,\omega}$, $A_{k,\omega}$ and $a_{k,\omega}$).

1.3 Wavelet analysis of time series

A continuous wavelet analysis is applied in time. The continuous wavelet transform considered here is the one described by Torrence and Compo (1998), which is arguably the most widely used wavelet technique in atmospheric science. One advantage of the 'continuous' (in contrast to 'discrete') wavelet transform is that the user can arbitrarily select the frequency resolution of the output spectrum. This is helpful especially in investigating traveling planetary waves, as the user has no prior knowledge of the dominant frequency of the wave. On the other hand, the discrete wavelet transform has its own advantage such as non-redundancy and straightforward invertibility (e.g., Yano et al., 2001, 2004), which, however, will not be explored in this study.

For a given time series $x(t)$, the continuous wavelet transform X is defined as the convolution of $x(t)$ with a wavelet function Ψ:

$$X(s,\tau) = \int_{-\infty}^{\infty} x(t)\Psi^*\left(\frac{t-\tau}{s}\right) dt, \tag{16}$$

where s is the scaling factor, representing the extent of dilation or compression of the wavelet, and τ is the translation factor, representing time shift. Ψ^* is the complex conjugate of Ψ. For the present study, the Morlet wavelet is used for Ψ. The Morlet wavelet is the product of a complex sinusoid and a Gaussian window. That is,

$$\Psi\left(\frac{t}{s}\right) = \left(\cos\frac{\omega_0 t}{s} + i\sin\frac{\omega_0 t}{s}\right) e^{-\frac{1}{2}\left(\frac{t}{s}\right)^2}. \tag{17}$$

ω_0 is usually set to be 6 to satisfy the admissibility condition (e.g., Farge et al., 1992).

If $x(t)$ is sampled with the sampling interval Δt for a finite length in time from t_0 to t_{N-1},

$$t_n = n\Delta t \tag{18}$$

$$x_n = x(n\Delta t) \tag{19}$$

$$\Psi_{n,s} = \Psi\left(\frac{n\Delta t}{s}\right) \tag{20}$$

where $n = \{0, 1, 2, ..., N-1\}$, and N is the number of points in the time series. The scaling factor s can be arbitrarily selected. Torrence and Compo (1998) used a set of scales that is fractional powers of two, and it is also adopted here. That is,

$$s_j = s_0 2^{j\Delta j} \tag{21}$$

where $s_0 = 2\Delta t$ and $j = \{0, 1, 2, ..., J\}$. Δj controls the scale resolution, which the user can arbitrarily select. J determines the largest scale and is given by

$$J = \frac{1}{\Delta j} \log_2 \left(\frac{N}{2} \right). \tag{22}$$

The wavelet transform (16) can be approximated as follows:

$$X_{n,s} = X(s, n\Delta t) = \sum_{n'=0}^{N-1} x_{n'} \Psi^*_{n'-n,s} \tag{23}$$

In practical application, the equation (23) is not directly used for the computation of X. Instead, the Fourier transforms of x and Ψ are used in light of the convolution theorem. The convolution theorem states that the Fourier transform of a convolution of two functions is the same as the product of the Fourier transforms of the two functions. The discrete Fourier transform of x is:

$$\hat{x}_m = \mathcal{F}\{x_n\} = \sum_{n=0}^{N-1} x_n e^{-i\frac{mn}{N}}, \tag{24}$$

where $m = \{0, 1, 2, ..., N-1\}$ is the frequency index, and $\mathcal{F}$ is the Fourier transform operator. The Fourier transform of the Morlet wavelet Ψ is:

$$\hat{\Psi}(s\omega) = H(\omega) e^{-\frac{(s\omega - \omega_0)^2}{2}}, \tag{25}$$

where $H(\omega) = 1$ for $\omega > 0$, and $H(\omega) = 0$ for $\omega \leq 0$. The discrete Fourier transform is

$$\hat{\Psi}_m = \mathcal{F}\{\Psi_n\} = \hat{\Psi}(s\omega_m), \tag{26}$$

where

$$\omega_m = \frac{2\pi m}{N\Delta t} \quad (m \leq \frac{N}{2}) \tag{27}$$

$$\omega_m = -\frac{2\pi m}{N\Delta t} \quad (m > \frac{N}{2}). \tag{28}$$

Based on the convolution theorem, the convolution integral of the two functions is the inverse Fourier transform of the product of the Fourier transforms of the two functions. Thus, the equation (23) can be written as:

$$X_{n,s} = \mathcal{F}^{-1}\{\hat{x}_m \hat{\Psi}_m\}, \tag{29}$$

where $\mathcal{F}^{-1}$ is the operator for the inverse Fourier transform. Thanks to the fast Fourier transform (FFT) algorithm (e.g., Frigo and Johnson, 1998), the computation of (29) is much faster than the computation of (23).

A wavelet spectrum can be obtained by plotting the amplitude $|X_{n,s}|$ or power $|X_{n,s}|^2$ of the wavelet transform as a function of time (i.e., $n\Delta t$) and wave period (or scale s). According to Meyers et al. (1993), there is a simple relationship between the wave period T and Morlet wavelet scale s:

$$T = \frac{4\pi}{\omega_0 + \sqrt{\omega_0 + 2}} s. \tag{30}$$

Thus, $T = 1.03\ s$ for ω_0=6.

1.4 Fourier-wavelet analysis

As described in 1.2, Hayashi's method involves two steps. The first step is the Fourier transform of space-time data in longitude, and the second step is the Fourier transform of the obtained Fourier coefficients in time. This paper explains how the second step (Fourier analysis in time) can be replaced by the wavelet analysis. It should be noted that the idea of using the wavelet technique in space-time analysis itself is not new. For instance, Alexander and Shepherd (2010) used the method of Hayashi (1971) to determine the amplitude of eastward- and westward-propagating global-scale waves with different zonal wavenumbers, and then applied the wavelet analysis to the amplitude time series. Mukhtarov et al. (2010) performed least-squares fits of functions in the form of $R_{k,\omega} \cos(\omega t - k\lambda - \phi_{k,\omega})$ tapered by a Gaussian window. They called their technique 'wavelet-periodogram method'. Kikuchi and Wang (2010) used a 2-D wavelet transform to analyze longitude-time data, which enables to identify wave activity that is localized not only in time but also in space. Kikuchi (2014) introduced a simpler version of the technique called 'combined Fourier-wavelet (CFW) transform', which involves the Fourier transform in longitude and wavelet transform in time. Kikuchi (2014) provided a Fortran software. However, since the main focus of Kikuchi (2014) was on the introduction of the CFW concept, rather than the implementation technique, the application of the CFW technique is still generally challenging for non-Fortran users.

The present study introduces a method to derive global-scale wave spectra, which are similar to those from the CFW analysis. The technique is referred to as 'Fourier-wavelet' analysis without the term 'combined', because in the present approach, the Fourier and wavelet transforms are two independent operations. The Fourier-wavelet technique is easy to implement using existing software of Fourier and wavelet transforms, which are readily available in many data analysis software such as Matlab. A Fourier-wavelet spectrum obtained from this analysis gives the amplitude and phase of the wave as a function of time and wave period, similar to a wavelet spectrum but separately for eastward- and westward-propagating waves with different zonal wavenumbers.

2 Methodology

In Hayashi's method, the wave amplitude is assumed to be constant. In order to taken into account localization of wave activity, the sinusoids in (3) and (4) are replaced by Gaussian-modulated sinusoids. That is,

$$\delta W_k'^+ = \sum_\omega R_{k,\omega}'^+ e^{-\frac{1}{2}\left(\frac{t}{s}\right)^2} \cos\left(\omega t - k\lambda - \varphi_{k,\omega}'^+\right) \tag{31}$$

200 and

$$\delta W_k'^- = \sum_\omega R_{k,\omega}'^- e^{-\frac{1}{2}\left(\frac{t}{s}\right)^2} \cos\left(\omega t + k\lambda - \varphi_{k,\omega}'^-\right) \tag{32}$$

Accordingly, (6) and (7) are modified as follows:

$$C_k'(t) = \sum_\omega \left(A_{k,\omega}' e^{-\frac{1}{2}\left(\frac{t}{s}\right)^2}\cos\omega t + B_{k,\omega}' e^{-\frac{1}{2}\left(\frac{t}{s}\right)^2}\sin\omega t\right) \tag{33}$$

$$S_k'(t) = \sum_\omega \left(a_{k,\omega}' e^{-\frac{1}{2}\left(\frac{t}{s}\right)^2}\cos\omega t + b_{k,\omega}' e^{-\frac{1}{2}\left(\frac{t}{s}\right)^2}\sin\omega t\right). \tag{34}$$

205 In analogy to Hayashi's formulas (8–15), the coefficients $A_{k,\omega}'$, $B_{k,\omega}'$, $a_{k,\omega}'$ and $b_{k,\omega}'$ are related to $R_{k,\omega}'^\pm$ and $\varphi_{k,\omega}'^\pm$ as follows:

$$R_{k,\omega}'^\pm = \frac{1}{2}\sqrt{\left(A_{k,\omega}' \pm b_{k,\omega}'\right)^2 + \left(B_{k,\omega}' \mp a_{k,\omega}'\right)^2} \tag{35}$$

$$\varphi_{k,\omega}'^\pm = \arctan\frac{B_{k,\omega}' \mp a_{k,\omega}'}{A_{k,\omega}' \pm b_{k,\omega}'}. \tag{36}$$

Using (17), equations (33) and (34) can be expressed as:

$$C_k'(t) = \sum_\omega \left(A_{k,\omega}'\Re(\Psi^*) - B_{k,\omega}'\Im(\Psi^*)\right) \tag{37}$$

210 $$S_k'(t) = \sum_\omega \left(a_{k,\omega}'\Re(\Psi^*) - b_{k,\omega}'\Im(\Psi^*)\right), \tag{38}$$

where $\Re(\Psi^*)$ and $\Im(\Psi^*)$ represent the real and imaginary parts of Ψ^*, respectively. Just like $A_{k,\omega}$ and $B_{k,\omega}$ which can be obtained as the cosine and sine coefficients of the Fourier transform of C_k (see (6)), $A_{k,\omega}'$ and $B_{k,\omega}'$ can be obtained as the real and negative imaginary coefficients of the wavelet transform of C_k'. Similarly, $a_{k,\omega}'$ and $b_{k,\omega}'$ can be obtained as the real and negative imaginary coefficients of the wavelet transform of S_k'.

215 In summary, the amplitude R' and phase φ' of eastward $(+)$ and westward $(-)$ propagating wave components with zonal wavenumber k and frequency ω can be determined in the following two steps. The first step is the Fourier transform of longitude-time data in longitude, which gives the time series of the cosine and sine Fourier coefficients (i.e., $C_k'(t)$ and $S_k'(t)$). The second step is the wavelet transform of $C_k'(t)$ and $S_k'(t)$ in time. The real part of the wavelet coefficients of $C_k'(t)$ and $S_k'(t)$ gives $A_{k,\omega}'$ and $a_{k,\omega}'$, respectively; and the negative imaginary part of the wavelet coefficients of $C_k'(t)$ and $S_k'(t)$ gives 220 $B_{k,\omega}'$ and $b_{k,\omega}'$, respectively. Once $A_{k,\omega}'$, $B_{k,\omega}'$, $a_{k,\omega}'$ and $b_{k,\omega}'$ are determined, $R_{k,\omega}'^\pm$ and $\varphi_{k,\omega}'^\pm$ can be derived using (35) and (36).

The implementation of the technique is easy, as it requires only standard Fourier and wavelet tools. Matlab and Python software are created and made available at [https://igit.iap-kborn.de/yamazaki/fourierwavelet] that compute $R_{k,\omega}'^\pm$ and $\varphi_{k,\omega}'^\pm$ for input data evenly gridded in time and longitude. For the Fourier analysis, the FFT algorithm is used when there are no missing values in the input data; otherwise, the least-squares method (e.g., Wells et al., 1985) is used, which allow gaps in the input data.

225 The wavelet analysis is based on the software provided by Torrence and Compo (1998), which outputs not only the wavelet transform but also other useful parameters such as the 'cone of influence' and the threshold for the 95% confidence level.

3 Application examples

In this section, examples are presented for the application of the Fourier-wavelet analysis to space-time data. The first example uses synthetic data, for which the exact wave composition is known. In the other examples, longitude-time data from atmospheric models are analyzed to demonstrate that the technique can be used to identify global-scale waves in the MLT region. For the analysis of atmospheric waves, special attention is paid to sudden stratospheric warming events, where tides and traveling planetary waves in the MLT region often show a large response. The events that are well documented in the literature are selected.

3.1 Analysis of synthetic data

A 2-D data matrix is created that mimics longitude-time data containing global-scale waves. The data, presented in Figure 1a, consist of two wave components, namely 'wave_A' and 'wave_B', along with noise. The wave_A is westward-propagating with zonal wavenumber k=2 (W2) and the wave_B is eastward-propagating with zonal wavenumber k=3 (E3). Notations such as W2 and E3 are used in the remainder of this paper, where 'W' and 'E' denote westward- and eastward-propagating components, respectively, and the number that follows W or E represents the zonal wavenumber k.

The amplitude of wave_A is depicted in the upper panel of Figure 1b. It changes between 0 and 1 over time in an arbitrary manner. The period of wave_A also changes over time, as shown in Figure 1c. Also presented in Figure 1c is the amplitude of W2 derived using the Fourier-wavelet method. The white curves indicate the 95% significance level estimated using the method described by Torrence and Compo (1998). The white dashed lines show the cone of influence, outside of which the edge effect may not be negligible. The Fourier-wavelet spectrum successfully identifies spectral peaks at the period of wave_A. The spectral amplitude tends to exceed the significance threshold when the amplitude of wave_A is above 0. Figure 1d is the same as Figure 1c but derived with the least-squares fitting method, which is often used for studying global-scale waves in the MLT region (e.g., Fan et al., 2022; Qin et al., 2022). The analysis was performed using time windows that are 3 times the wave period, which is a common choice in investigations of traveling planetary waves (e.g., Forbes and Zhang, 2015; Yamazaki and Matthias, 2019). The amplitude is not computed at the beginning and end of the data, where the length of the data is less than 3 times the wave period. There is good agreement between the results derived with the Fourier-wavelet (Figure 1c) and least-squares fitting (Figure 1d) methods. However, the computation time for the Fourier-wavelet method is approximately $\frac{1}{100}$ that for the least-squares fitting method, highlighting the advantage of the Fourier-wavelet method in computation speed. Figures 1e–1g correspond to Figures 1b–1d but for wave_B. Again, the Fourier-wavelet spectrum succeeds to identify the amplitude and period of wave_B.

3.2 GAIA simulation: Tides and traveling planetary waves during August–October 2019

There was an Antarctic sudden stratospheric warming in September 2019 (Lim et al., 2020; Rao et al., 2020; Yamazaki et al., 2020a). Although this event is categorized as a 'minor' warming (i.e., no reversal of the zonal mean flow at 10 hPa), it was unusually strong for a Southern-Hemisphere event in various measures (Lim et al., 2021), and its effects were observed at

different layers of the atmosphere (e.g., Goncharenko et al., 2020; Noguchi et al., 2020; Safieddine et al., 2020; Wargan et al., 2020; Yamazaki et al., 2020a). A global simulation of the September 2019 sudden stratospheric warming event was presented by Miyoshi and Yamazaki (2020) based on the whole atmosphere model GAIA. GAIA stands for the Ground-to-Topside Model of Atmosphere and Ionosphere for Aeronomy, and detailed model descriptions can be found in Jin et al. (2011) and Miyoshi et al. (2017). Figure 2a shows the polar stratospheric temperature and zonal mean zonal wind velocity at $60°$N at 10 hPa during August–October, as derived from the GAIA model. A rapid increase of the polar temperature in September and concurrent reduction of the zonal mean zonal wind velocity are evident, which indicates the occurrence of the sudden stratospheric warming. Since the model is constrained by the JRA55 reanalysis (Kobayashi et al., 2015) below a height of 40 km, these results strongly reflect the JRA55 predictions.

Figure 2b depicts hourly values of the zonal wind velocity over the equator at an altitude of 100 km as a function of time and longitude. The zonal wind velocity shows considerable variability within the range of ±200 m/s, which is mostly due to waves generated in the region below 40 km. Figures 2c–2h show Fourier-wavelet spectra of the equatorial zonal wind velocity at 100 km for different wave components.

In Figure 2c, the amplitude of the W1 component at a period T of ~6 days is enhanced around Days 40–70. Earlier studies found that the amplitude of the Q6DW (W1, $T\sim6$ days) during the September 2019 sudden stratospheric warming was unusually large compared to its seasonal climatology and had a significant impact on the ionosphere (Lin et al., 2020; Gu et al., 2021; Lee et al., 2021; Ma et al., 2022; Qin et al., 2021a; Yamazaki et al., 2020a; Miyoshi and Yamazaki, 2020; Mitra et al., 2022). In Figure 2e, there is also a hint of the enhanced Q4DW (W2, $T\sim4$ days) and Q7DW (W2, $T\sim7$ days) around the same time.

In Figure 2d, the UFKW (E1, $T\sim3.5$ days) is seen throughout the period. In Figure 2g, the Q2DW (W3, $T\sim2$ days) is seen at the beginning of August 2019, but its amplitude is below the significance threshold. Their wave activity seems unrelated to the occurrence of the sudden stratospheric warming. Also, there is no apparent correlation between the sudden stratospheric warming and tidal activity. The most prominent tidal mode in these figures is DE3 (Figure 2h). The amplitude of DE3 is known to be largest during August–October (e.g., Zhang et al., 2006; Akmaev et al., 2008; Yamazaki et al., 2023).

3.3 SD/WACCM-X simulation: Tidal variability during January–February 2009

A 'major' Arctic sudden stratospheric warming occurred in January 2009 (Manney et al., 2009; Harada et al., 2010). Whole atmosphere simulations of this event were presented by several authors (e.g., Fuller-Rowell et al., 2011; Jin et al., 2012; Sassi et al., 2013; Pedatella et al., 2014; Siddiqui et al., 2021). Siddiqui et al. (2021) used the Whole Atmosphere Community Climate Model with thermosphere and ionosphere extension (WACCM-X) (Liu et al., 2018) with specified dynamics (SD), in which the region below 50 km is constrained by the Modern Era Retrospective Analysis for Research and Applications Version 2 (MERRA-2) (Gelaro et al., 2017). The polar temperature and zonal mean zonal wind velocity at $60°$N at 10 hPa derived from this SD/WACCM-X simulation are plotted in Figure 3a for the period of January–February 2009. The reversal of the zonal mean flow is seen on Day 23, confirming that this event is a major warming.

Observational studies have found large semidiurnal variations in the ionosphere during the January 2009 sudden stratospheric warming (Goncharenko et al., 2010a, b; Fejer et al., 2010; Yue et al., 2010). Numerical studies clarified that the semidiurnal ionospheric variations are due to the enhancement of semidiurnal tides that are generated in the lower atmosphere and propagate into the ionosphere (Jin et al., 2012; Wang et al., 2014; Pedatella et al., 2014). Figure 3b shows the W2 component of the Fourier-wavelet spectrum for the zonal wind velocity at 50°N and 110 km. An enhancement of SW2 (W2, T=12 h) is clearly visible following the reversal of the zonal mean flow. By performing the Fourier-wavelet analysis at different latitudes, it is possible to visualize the global structure of SW2 (Figure 3c). It can be seen from Figure 3c that the amplitude of SW2 increased and decreased in the Northern and Southern Hemispheres, respectively, during the sudden stratospheric warming. A similar plot is shown in Figure 3d but for DW1 (W1, T=24 h) and at 95 km, where the amplitude of DW1 is largest. The relationship between sudden stratospheric warmings and DW1 tidal variability was discussed in Siddiqui et al. (2022).

3.4 SD/WACCM-X simulation: Traveling planetary waves during January–May 2016

A sudden stratospheric warming that coincides with the spring transition is called a 'final' warning (e.g, Black and McDaniel, 2007; Matthias et al., 2021). Studies have noted that a final warming event is often accompanied by a strong Q10DW (W1, T∼10 days) in the MLT region (Yamazaki and Matthias, 2019; Yu et al., 2019; Yin et al., 2022; Qin et al., 2022). Examples include the final warming event in March 2016. Figure 4a shows the polar temperature and zonal mean zonal wind velocity at 10 hPa as obtained from the SD/WACCM-X simulation presented by Gasperini et al. (2020). The direction of the zonal mean flow reversed from eastward to westward on Day 65, and did not turn back eastward until the next winter.

Figure 4b displays daily values of the geopotential height at 0.01 hPa (∼77 km) as a function of time and longitude, where a westward-propagating wave-like perturbation is visible during the final warming. The W1 and E1 components of the Fourier-wavelet spectrum obtained from these data are presented in Figures 4c and 4d, respectively. A burst of the Q10DW (W1, T∼10 days) during the final warming can be easily identified in the W1 spectrum (Figure 4c). The height profiles of the amplitude and phase of the Q10DW are depicted in Figures 4e and 4f, respectively, for Day 72. The peak of the amplitude is seen at ∼70 km. The downward phase propagation (Figure 4f) is consistent with the upward energy propagation of the Q10DW. The characteristics of the Q10DW during the March 2016 final warming derived with the Fourier-wavelet method are in good agreement with the observations presented by Yamazaki and Matthias (2019) based on the least-squares fitting technique.

As a brief summary, the results presented in Sections 3.2–3.4 demonstrate that global-scale wave spectra derived using the Fourier-wavelet method described in Section 2 are useful for identifying various types of tides and traveling planetary waves in the MLT region and their temporal variability. The structures of the global-scale waves can be determined by performing the Fourier-wavelet analysis at different latitudes and heights.

4 Conclusions

This study describes a simple method for deriving Fourier-wavelet spectra from 2-D longitude-time data. The method is conceptually similar to that of Hayashi (1971), which first performs the Fourier analysis in longitude, then performs the Fourier

analysis in time. In the proposed technique, the Fourier analysis in time is replaced by the wavelet analysis (Torrence and
325 Compo, 1998), which can resolve wave activity localized in time. Briefly, the implementation of the technique involves two steps. In the first step, the Fourier transform is performed in longitude, and time series of the sine and cosine Fourier coefficients are derived. In the second step, the wavelet transform is performed on these time series, and real and imaginary wavelet coefficients are derived. Using these wavelet coefficients, Fourier-wavelet spectra can be obtained separately for eastward- and westward-propagating waves with different zonal wavenumbers (see Section 2 for details).

330 Matlab and Python software for computing Fourier-wavelet spectra are created and made available at [https://igit.iap-kborn. de/yamazaki/fourierwavelet]. Application examples, based on these Fourier-wavelet software, are presented in Section 3. The results suggest that the technique can successfully identify tides and traveling planetary waves in the mesosphere and lower thermosphere (MLT) region and their transient response to sudden stratospheric warming events (Sections 3.2–3.4). The Fourier-wavelet method has an advantage over other existing methods in that the computation is fast. For the example presented
335 in Section 3.1, the computation time for the Fourier-wavelet method is approximately $\frac{1}{100}$ that for the least-squares fitting method.

Although this study has focused on tides and traveling planetary waves in the MLT region, the Fourier-wavelet method can be easily applied to data from other regions of the atmosphere. Also, the applicability of the technique in research areas outside atmospheric science is yet to be explored.

340 *Code and data availability.* Matlab and Python software (fourierwavelet v1.1) for computing Fourier-wavelet spectra are available at URL: [https://igit.iap-kborn.de/yamazaki/fourierwavelet] under the GNU General Public License. They can also be downloaded from the Zenodo website at [https://doi.org/10.5281/zenodo.8033686] along with additional Matlab software that reproduce Figures 1–4. Matlab wavelet software was provided by C. Torrence and G. Compo under the MIT license, and is available at URL: [http://atoc.colorado.edu/research/wavelets/]. Python wavelet software was created by Evgeniya Predybaylo and Michael von Papen based on Torrence and Compo (1998), and
345 is also available at the same URL. The GAIA simulation data used in Section 3.2 are available from GFZ Data Services [https://doi.org/10.5880/GFZ.2.3.2020.004]. The SD/WACCM-X simulation data used in Section 3.3 are available from [https://data.mendeley.com/datasets/47pnw8pgmk/1]. The SD/WACCM-X simulation data used in Section 3.4 are available from [https://doi.org/10.26024/5b58-nc53].

Author contributions. YY was in charge of conceptualizing the study, data analysis, visualization of the results, writing the manuscript, and creating the Matlab and Python scripts.

350 *Competing interests.* The author declares that he has no conflict of interest.

Acknowledgements. The author was supported by the Deutsche Forschungsgemeinschaft (DFG) grant YA-574-3-1.

References

Akmaev, R., Fuller-Rowell, T., Wu, F., Forbes, J., Zhang, X., Anghel, A., Iredell, M., Moorthi, S., and Juang, H.-M.: Tidal variability in the lower thermosphere: Comparison of Whole Atmosphere Model (WAM) simulations with observations from TIMED, Geophys. Res. Lett., 35, https://doi.org/doi:10.1029/2007GL032584, 2008.

Alexander, S. and Shepherd, M.: Planetary wave activity in the polar lower stratosphere, Atmos. Chem. Phys., 10, 707–718, https://doi.org/10.5194/acp-10-707-2010, 2010.

Baldwin, M. P., Ayarzagüena, B., Birner, T., Butchart, N., Butler, A. H., Charlton-Perez, A. J., Domeisen, D. I., Garfinkel, C. I., Garny, H., Gerber, E. P., et al.: Sudden stratospheric warmings, Rev. Geophys., 59, e2020RG000 708, https://doi.org/10.1029/2020RG000708, 2021.

Butler, A. H., Seidel, D. J., Hardiman, S. C., Butchart, N., Birner, T., and Match, A.: Defining sudden stratospheric warmings, Bull. Am. Meteorol., 96, 1913–1928, https://doi.org/10.1175/BAMS-D-13-00173.1, 2015.

Chandran, A., Garcia, R., Collins, R., and Chang, L.: Secondary planetary waves in the middle and upper atmosphere following the stratospheric sudden warming event of January 2012, Geophys. Res. Lett., 40, 1861–1867, https://doi.org/10.1002/grl.50373, 2013.

Chang, L. C., Palo, S. E., and Liu, H.-L.: Short-term variability in the migrating diurnal tide caused by interactions with the quasi 2 day wave, J. Geophys. Res.: Atmospheres, 116, https://doi.org/10.1029/2010JD014996, 2011.

Davis, R. N., Chen, Y.-W., Miyahara, S., and Mitchell, N. J.: The climatology, propagation and excitation of ultra-fast Kelvin waves as observed by meteor radar, Aura MLS, TRMM and in the Kyushu-GCM, Atmos. Chem. Phys., 12, 1865–1879, https://doi.org/10.5194/acp-12-1865-2012, 2012.

Day, K. A., Hibbins, R. E., and Mitchell, N. J.: Aura MLS observations of the westward-propagating s= 1, 16-day planetary wave in the stratosphere, mesosphere and lower thermosphere, Atmos. Chem. Phys., 11, 4149–4161, https://doi.org/10.5194/acp-11-4149-2011, 2011.

Fan, Y., Huang, C. M., Zhang, S. D., Huang, K. M., and Gong, Y.: Long-Term Study of Quasi-16-day Waves Based on ERA5 Reanalysis Data and EOS MLS Observations From 2005 to 2020, J. Geophys. Res.: Space Physics, 127, e2021JA030 030, https://doi.org/10.1029/2021JA030030, 2022.

Farge, M. et al.: Wavelet transforms and their applications to turbulence, Annu. Rev. Fluid Mech., 24, 395–458, https://doi.org/10.1146/annurev.fl.24.010192.002143, 1992.

Fejer, B., Olson, M., Chau, J., Stolle, C., Lühr, H., Goncharenko, L., Yumoto, K., and Nagatsuma, T.: Lunar-dependent equatorial ionospheric electrodynamic effects during sudden stratospheric warmings, J. Geophys. Res.: Space Physics, 115, https://doi.org/10.1029/2010JA015273, 2010.

Forbes, J., Hagan, M., Miyahara, S., Vial, F., Manson, A., Meek, C., and Portnyagin, Y. I.: Quasi 16-day oscillation in the mesosphere and lower thermosphere, J. Geophys. Res.: Atmospheres, 100, 9149–9163, https://doi.org/10.1029/94JD02157, 1995a.

Forbes, J., Zhang, X., Palo, S., Russell, J., Mertens, C., and Mlynczak, M.: Tidal variability in the ionospheric dynamo region, J. Geophys. Res.: Space Physics, 113, https://doi.org/10.1029/2007JA012737, 2008.

Forbes, J. M.: Atmospheric tides: 1. Model description and results for the solar diurnal component, J. Geophys. Res.: Space Physics, 87, 5222–5240, https://doi.org/10.1029/JA087iA07p05222, 1982a.

Forbes, J. M.: Atmospheric tide: 2. The solar and lunar semidiurnal components, J. Geophys. Res.: Space Physics, 87, 5241–5252, https://doi.org/10.1029/JA087iA07p05241, 1982b.

Forbes, J. M.: Middle atmosphere tides, J. Atmos. Terr. Phys., 46, 1049–1067, https://doi.org/10.1016/0021-9169(84)90008-4, 1984.

Forbes, J. M. and Zhang, X.: Quasi-10-day wave in the atmosphere, J. Geophys. Res.: Atmospheres, 120, 11–079, https://doi.org/10.1002/2015JD023327, 2015.

390 Forbes, J. M. and Zhang, X.: The quasi-6 day wave and its interactions with solar tides, J. Geophys. Res.: Space Physics, 122, 4764–4776, https://doi.org/10.1002/2017JA023954, 2017.

Forbes, J. M., Zhang, X., Palo, S. E., Russell, J., Mertens, C. J., and Mlynczak, M.: Kelvin waves in stratosphere, mesosphere and lower thermosphere temperatures as observed by TIMED/SABER during 2002–2006, Earth, Planets and Space, 61, 447–453, https://doi.org/10.1186/BF03353161, 2009.

395 Forbes, J. M. et al.: Tidal and planetary waves, The Upper Mesosphere and Lower Thermosphere: A Review of Experiment and Theory, Geophys. Monogr. Ser, 87, 67–87, https://doi.org/10.1029/GM087p0067, 1995b.

Frigo, M. and Johnson, S. G.: FFTW: An adaptive software architecture for the FFT, in: Proceedings of the 1998 IEEE International Conference on Acoustics, Speech and Signal Processing, ICASSP'98 (Cat. No. 98CH36181), vol. 3, pp. 1381–1384, IEEE, https://doi.org/10.1109/ICASSP.1998.681704, 1998.

400 Fuller-Rowell, T., Wu, F., Akmaev, R., Fang, T.-W., and Araujo-Pradere, E.: A whole atmosphere model simulation of the impact of a sudden stratospheric warming on thermosphere dynamics and electrodynamics, J. Geophys. Res.: Space Physics, 115, https://doi.org/10.1029/2010JA015524, 2010.

Fuller-Rowell, T., Wang, H., Akmaev, R., Wu, F., Fang, T.-W., Iredell, M., and Richmond, A.: Forecasting the dynamic and electrodynamic response to the January 2009 sudden stratospheric warming, Geophys. Res. Lett., 38, https://doi.org/10.1029/2011GL047732, 2011.

405 Gan, Q., Oberheide, J., and Pedatella, N. M.: Sources, sinks, and propagation characteristics of the quasi 6-day wave and its impact on the residual mean circulation, J. Geophys. Res.: Atmospheres, 123, 9152–9170, https://doi.org/10.1029/2018JD028553, 2018.

Gan, Q., Eastes, R. W., Burns, A. G., Wang, W., Qian, L., Solomon, S. C., Codrescu, M. V., and McClintock, W. E.: New observations of large-scale waves coupling with the ionosphere made by the GOLD Mission: Quasi-16-day wave signatures in the F-region OI 135.6-nm nightglow during sudden stratospheric warmings, J. Geophys. Res.: Space Physics, 125, e2020JA027 880,

410 https://doi.org/10.1029/2020JA027880, 2020.

Gasperini, F., Forbes, J., Doornbos, E., and Bruinsma, S.: Wave coupling between the lower and middle thermosphere as viewed from TIMED and GOCE, J. Geophys. Res.: Space Physics, 120, 5788–5804, https://doi.org/doi.org/10.1002/2015JA021300, 2015.

Gasperini, F., Liu, H., and McInerney, J.: Preliminary evidence of Madden-Julian Oscillation effects on ultrafast tropical waves in the thermosphere, J. Geophys. Res.: Space Physics, 125, e2019JA027 649, https://doi.org/10.1029/2019JA027649, 2020.

415 Gelaro, R., McCarty, W., Suárez, M. J., Todling, R., Molod, A., Takacs, L., Randles, C. A., Darmenov, A., Bosilovich, M. G., Reichle, R., et al.: The modern-era retrospective analysis for research and applications, version 2 (MERRA-2), J. Clim., 30, 5419–5454, https://doi.org/10.1175/JCLI-D-16-0758.1, 2017.

Goncharenko, L., Chau, J., Liu, H.-L., and Coster, A.: Unexpected connections between the stratosphere and ionosphere, Geophys. Res. Lett., 37, https://doi.org/10.1029/2010GL043125, 2010a.

420 Goncharenko, L., Coster, A., Chau, J., and Valladares, C.: Impact of sudden stratospheric warmings on equatorial ionization anomaly, J. Geophys. Res.: Space Physics, 115, https://doi.org/10.1029/2010JA015400, 2010b.

Goncharenko, L. P., Harvey, V. L., Greer, K. R., Zhang, S.-R., and Coster, A. J.: Longitudinally dependent low-latitude ionospheric disturbances linked to the Antarctic sudden stratospheric warming of September 2019, J. Geophys. Res.: Space Physics, 125, e2020JA028 199, https://doi.org/10.1029/2020JA028199, 2020.

425   Goncharenko, L. P., Harvey, V. L., Liu, H., and Pedatella, N. M.: Sudden Stratospheric Warming Impacts on the Ionosphere–Thermosphere System: A Review of Recent Progress, Ionosphere Dynamics and Applications, pp. 369–400, https://doi.org/10.1002/9781119815617.ch16, 2021.

Gu, S.-Y., Li, T., Dou, X., Wu, Q., Mlynczak, M., and Russell Iii, J.: Observations of quasi-two-day wave by TIMED/SABER and TIMED/-TIDI, J. Geophys. Res.: Atmospheres, 118, 1624–1639, https://doi.org/10.1002/jgrd.50191, 2013.

430   Gu, S.-Y., Dou, X., Lei, J., Li, T., Luan, X., Wan, W., and Russell III, J.: Ionospheric response to the ultrafast Kelvin wave in the MLT region, J. Geophys. Res.: Space Physics, 119, 1369–1380, https://doi.org/10.1002/2013JA019086, 2014.

Gu, S.-Y., Liu, H.-L., Dou, X., and Li, T.: Influence of the sudden stratospheric warming on quasi-2-day waves, Atmos. Chem. Phys., 16, 4885–4896, https://doi.org/10.5194/acp-16-4885-2016, 2016.

Gu, S.-Y., Teng, C.-K.-M., Li, N., Jia, M., Li, G., Xie, H., Ding, Z., and Dou, X.: Multivariate analysis on the ionospheric
435   responses to planetary waves during the 2019 Antarctic SSW event, J. Geophys. Res.: Space Physics, 126, e2020JA028 588, https://doi.org/10.1029/2020JA028588, 2021.

Hagan, M. and Forbes, J.: Migrating and nonmigrating diurnal tides in the middle and upper atmosphere excited by tropospheric latent heat release, J. Geophys. Res.: Atmospheres, 107, ACL–6, https://doi.org/10.1029/2001JD001236, 2002.

Harada, Y., Goto, A., Hasegawa, H., Fujikawa, N., Naoe, H., and Hirooka, T.: A major stratospheric sudden warming event in January 2009,
440   J. Atmos. Sci., 67, 2052–2069, https://doi.org/10.1175/2009JAS3320.1, 2010.

Hayashi, Y.: A generalized method of resolving disturbances into progressive and retrogressive waves by space Fourier and time cross-spectral analyses, J. Meteorol. Soc. Japan. Ser. II, 49, 125–128, https://doi.org/10.2151/jmsj1965.49.2_125, 1971.

He, M., Yamazaki, Y., Hoffmann, P., Hall, C. M., Tsutsumi, M., Li, G., and Chau, J. L.: Zonal Wave Number Diagnosis of Rossby Wave-Like Oscillations Using Paired Ground-Based Radars, J. Geophys. Res.: Atmospheres, 125, e2019JD031 599,
445   https://doi.org/10.1029/2019JD031599, 2020.

He, M., Chau, J. L., Forbes, J. M., Zhang, X., Englert, C. R., Harding, B. J., Immel, T. J., Lima, L. M., Bhaskar Rao, S. V., Ratnam, M. V., et al.: Quasi-2-day wave in low-latitude atmospheric winds as viewed from the ground and space during January–March, 2020, Geophys. Res. Lett., 48, e2021GL093 466, https://doi.org/10.1029/2021GL093466, 2021.

Hirooka, T. and Hirota, I.: Normal mode Rossby waves observed in the upper stratosphere. Part II: Second antisym-
450   metric and symmetric modes of zonal wavenumbers 1 and 2, J. Atmos. Sci., 42, 536–548, https://doi.org/10.1175/1520-0469(1985)042<0536:NMRWOI>2.0.CO;2, 1985.

Hirota, I. and Hirooka, T.: Normal mode Rossby waves observed in the upper stratosphere. Part I: First symmetric modes of zonal wavenumbers 1 and 2, J. Atmos. Sci., 41, 1253–1267, https://doi.org/10.1175/1520-0469(1984)041<1253:NMRWOI>2.0.CO;2, 1984.

Holton, J. R. and Lindzen, R. S.: A note on "Kelvin" waves in the atmosphere, Mon. Weather Rev., 96, 385–386, https://doi.org/10.1175/1520-
455   0493(1968)096<0385:ANOKWI>2.0.CO;2, 1968.

Huang, C., Li, W., Zhang, S., Chen, G., Huang, K., and Gong, Y.: Investigation of dominant traveling 10-day wave components using long-term MERRA-2 database, Earth, Planets and Space, 73, 1–12, https://doi.org/10.1186/s40623-021-01410-7, 2021.

Immel, T., Sagawa, E., England, S., Henderson, S., Hagan, M., Mende, S., Frey, H., Swenson, C., and Paxton, L.: Control of equatorial ionospheric morphology by atmospheric tides, Geophys. Res. Lett., 33, https://doi.org/10.1029/2006GL026161, 2006.

460   Jin, H., Miyoshi, Y., Fujiwara, H., Shinagawa, H., Terada, K., Terada, N., Ishii, M., Otsuka, Y., and Saito, A.: Vertical connection from the tropospheric activities to the ionospheric longitudinal structure simulated by a new Earth's whole atmosphere-ionosphere coupled model, J. Geophys. Res.: Space Physics, 116, https://doi.org/10.1029/2010JA015925, 2011.

Jin, H., Miyoshi, Y., Pancheva, D., Mukhtarov, P., Fujiwara, H., and Shinagawa, H.: Response of migrating tides to the stratospheric sudden warming in 2009 and their effects on the ionosphere studied by a whole atmosphere-ionosphere model GAIA with COSMIC and TIMED/SABER observations, J. Geophys. Res.: Space Physics, 117, https://doi.org/10.1029/2012JA017650, 2012.

Kasahara, A.: Normal modes of ultralong waves in the atmosphere, Mon. Weather Rev., 104, 669–690, https://doi.org/10.1175/1520-0493(1976)104<0669:NMOUWI>2.0.CO;2, 1976.

Kikuchi, K.: An introduction to combined Fourier–wavelet transform and its application to convectively coupled equatorial waves, Clim. Dyn., 43, 1339–1356, https://doi.org/10.1007/s00382-013-1949-8, 2014.

Kikuchi, K. and Wang, B.: Spatiotemporal wavelet transform and the multiscale behavior of the Madden–Julian oscillation, J. Clim., 23, 3814–3834, https://doi.org/10.1175/2010JCLI2693.1, 2010.

Kobayashi, S., Ota, Y., Harada, Y., Ebita, A., Moriya, M., Onoda, H., Onogi, K., Kamahori, H., Kobayashi, C., Endo, H., et al.: The JRA-55 reanalysis: General specifications and basic characteristics, J. Meteorol. Soc. Japan. Ser. II, 93, 5–48, https://doi.org/10.2151/jmsj.2015-001, 2015.

Kumar, P. and Foufoula-Georgiou, E.: Wavelet analysis for geophysical applications, Rev. Geophys., 35, 385–412, https://doi.org/10.1029/97RG00427, 1997.

Laštovička, J.: Forcing of the ionosphere by waves from below, J. Atmos. Sol.-Terr. Phys., 68, 479–497, https://doi.org/10.1016/j.jastp.2005.01.018, 2006.

Lee, W., Song, I.-S., Kim, J.-H., Kim, Y. H., Jeong, S.-H., Eswaraiah, S., and Murphy, D.: The observation and SD-WACCM simulation of planetary wave activity in the middle atmosphere during the 2019 Southern Hemispheric sudden stratospheric warming, J. Geophys. Res.: Space Physics, 126, e2020JA029 094, https://doi.org/10.1029/2020JA029094, 2021.

Lieberman, R., Riggin, D., Ortland, D., Oberheide, J., and Siskind, D.: Global observations and modeling of nonmigrating diurnal tides generated by tide-planetary wave interactions, J. Geophys. Res.: Atmospheres, 120, 11–419, https://doi.org/10.1002/2015JD023739, 2015.

Lieberman, R. S. and Riggin, D.: High resolution Doppler imager observations of Kelvin waves in the equatorial mesosphere and lower thermosphere, J. Geophys. Res.: Atmospheres, 102, 26 117–26 130, https://doi.org/10.1029/96JD02902, 1997.

Lim, E.-P., Hendon, H. H., Butler, A. H., Garreaud, R. D., Polichtchouk, I., Shepherd, T. G., Scaife, A., Comer, R., Coy, L., Newman, P. A., et al.: The 2019 Antarctic sudden stratospheric warming, SPARC newsletter, 54, 10–13, https://www.sparc-climate.org/wp-content/uploads/sites/5/2017/12/SPARCnewsletter_Jan2020_WEB.pdf, 2020.

Lim, E.-P., Hendon, H. H., Butler, A. H., Thompson, D. W., Lawrence, Z. D., Scaife, A. A., Shepherd, T. G., Polichtchouk, I., Nakamura, H., Kobayashi, C., et al.: The 2019 Southern Hemisphere stratospheric polar vortex weakening and its impacts, Bull. Am. Meteorol., 102, E1150–E1171, https://doi.org/10.1175/BAMS-D-20-0112.1, 2021.

Lin, J., Lin, C., Rajesh, P., Yue, J., Lin, C., and Matsuo, T.: Local-time and vertical characteristics of quasi-6-day oscillation in the ionosphere during the 2019 Antarctic sudden stratospheric warming, Geophys. Res. Lett., 47, e2020GL090 345, https://doi.org/10.1029/2020GL090345, 2020.

Lindzen, R. S. and Chapman, S.: Atmospheric tides, Space Sci. Rev., 10, 3–188, https://doi.org/doi.org/10.1007/BF00171584, 1969.

Liu, H.-L.: Variability and predictability of the space environment as related to lower atmosphere forcing, Space Weather, 14, 634–658, https://doi.org/10.1002/2016SW001450, 2016.

Liu, H.-L., Talaat, E., Roble, R., Lieberman, R., Riggin, D., and Yee, J.-H.: The 6.5-day wave and its seasonal variability in the middle and upper atmosphere, J. Geophys. Res.: Atmospheres, 109, https://doi.org/10.1029/2004JD004795, 2004.

500   Liu, H.-L., Bardeen, C. G., Foster, B. T., Lauritzen, P., Liu, J., Lu, G., Marsh, D. R., Maute, A., McInerney, J. M., Pedatella, N. M., et al.: Development and validation of the Whole Atmosphere Community Climate Model with thermosphere and ionosphere extension (WACCM-X 2.0), J. Adv. Model. Earth Syst., 10, 381–402, https://doi.org/10.1002/2017MS001232, 2018.

Longuet-Higgins, M. S.: The eigenfunctions of Laplace's tidal equation over a sphere, Philos. Trans. R. Soc. A, 262, 511–607, https://doi.org/10.1098/rsta.1968.0003, 1968.

505   Luo, J., Ma, Z., Gong, Y., Zhang, S., Xiao, Q., Huang, C., and Huang, K.: Record-Strong Eastward Propagating 4-Day Wave in the Southern Hemisphere Observed During the 2019 Antarctic Sudden Stratospheric Warming, Geophysical Research Letters, 50, e2022GL102 704, 2023.

Ma, Z., Gong, Y., Zhang, S., Zhou, Q., Huang, C., Huang, K., Luo, J., Yu, Y., and Li, G.: Study of a Quasi 4-Day Oscillation During the 2018/2019 SSW Over Mohe, China, J. Geophys. Res.: Space Physics, 125, e2019JA027 687, https://doi.org/10.1029/2019JA027687, 510   2020.

Ma, Z., Gong, Y., Zhang, S., Xiao, Q., Xue, J., Huang, C., and Huang, K.: Understanding the Excitation of Quasi-6-Day Waves in Both Hemispheres During the September 2019 Antarctic SSW, J. Geophys. Res.: Atmospheres, 127, e2021JD035 984, https://doi.org/10.1029/2021JD035984, 2022.

Madden, R. A.: Large-scale, free Rossby waves in the atmosphere–An update, Tellus A, 59, 571–590, https://doi.org/10.1111/j.1600-515   0870.2007.00257.x, 2007.

Manney, G. L., Schwartz, M. J., Krüger, K., Santee, M. L., Pawson, S., Lee, J. N., Daffer, W. H., Fuller, R. A., and Livesey, N. J.: Aura Microwave Limb Sounder observations of dynamics and transport during the record-breaking 2009 Arctic stratospheric major warming, Geophys. Res. Lett., 36, https://doi.org/10.1029/2009GL038586, 2009.

Matsuno, T.: Quasi-geostrophic motions in the equatorial area, J. Meteorol. Soc. Japan. Ser. II, 44, 25–43, 520   https://doi.org/10.2151/jmsj1965.44.1_25, 1966.

Matthias, V., Hoffmann, P., Rapp, M., and Baumgarten, G.: Composite analysis of the temporal development of waves in the polar MLT region during stratospheric warmings, Journal of Atmospheric and Solar-Terrestrial Physics, 90, 86–96, 2012.

McDonald, A., Hibbins, R., and Jarvis, M.: Properties of the quasi 16 day wave derived from EOS MLS observations, J. Geophys. Res.: Atmospheres, 116, https://doi.org/10.1029/2010JD014719, 2011.

525   Mechoso, C. R. and Hartmann, D. L.: An observational study of traveling planetary waves in the Southern Hemisphere, J. Atmos. Sci., 39, 1921–1935, https://doi.org/10.1175/1520-0469(1982)039<1921:AOSOTP>2.0.CO;2, 1982.

Meyer, C. K. and Forbes, J.: A 6.5-day westward propagating planetary wave: Origin and characteristics, Journal of Geophysical Research: Atmospheres, 102, 26 173–26 178, 1997.

Meyers, S. D., Kelly, B. G., and O'Brien, J. J.: An introduction to wavelet analysis in oceanography and meteorology: With application to the 530   dispersion of Yanai waves, Mon. Weather Rev., 121, 2858–2866, https://doi.org/10.1175/1520-0493(1993)121<2858:AITWAI>2.0.CO;2, 1993.

Mitra, G., Guharay, A., Batista, P. P., and Buriti, R.: Impact of the September 2019 Minor Sudden Stratospheric Warming on the Low-Latitude Middle Atmospheric Planetary Wave Dynamics, J. Geophys. Res.: Atmospheres, 127, e2021JD035 538, https://doi.org/10.1029/2021JD035538, 2022.

535   Miyoshi, Y.: Temporal variation of nonmigrating diurnal tide and its relation with the moist convective activity, Geophys. Res. Lett., 33, https://doi.org/10.1029/2006GL026072, 2006.

Miyoshi, Y. and Fujiwara, H.: Day-to-day variations of migrating diurnal tide simulated by a GCM from the ground surface to the exobase, Geophys. Res. Lett., 30, https://doi.org/10.1029/2003GL017695, 2003.

Miyoshi, Y. and Fujiwara, H.: Excitation mechanism of intraseasonal oscillation in the equatorial mesosphere and lower thermosphere, J. Geophys. Res.: Atmospheres, 111, https://doi.org/10.1029/2003GL017695, 2006.

Miyoshi, Y. and Yamazaki, Y.: Excitation mechanism of ionospheric 6-day oscillation during the 2019 September sudden stratospheric warming event, J. Geophys. Res.: Space Physics, 125, e2020JA028 283, https://doi.org/10.1029/2020JA028283, 2020.

Miyoshi, Y., Pancheva, D., Mukhtarov, P., Jin, H., Fujiwara, H., and Shinagawa, H.: Excitation mechanism of non-migrating tides, J. Atmos. Sol.-Terr. Phys., 156, 24–36, https://doi.org/10.1016/j.jastp.2017.02.012, 2017.

Moldwin, M.: An introduction to space weather, Cambridge University Press, https://doi.org/10.1017/CBO9780511801365, 2022.

Moudden, Y. and Forbes, J.: Quasi-two-day wave structure, interannual variability, and tidal interactions during the 2002–2011 decade, J. Geophys. Res.: Atmospheres, 119, 2241–2260, https://doi.org/10.1002/2013JD020563, 2014.

Mukhtarov, P., Andonov, B., Borries, C., Pancheva, D., and Jakowski, N.: Forcing of the ionosphere from above and below during the Arctic winter of 2005/2006, J. Atmos. Sol.-Terr. Phys., 72, 193–205, https://doi.org/10.1016/j.jastp.2009.11.008, 2010.

Noguchi, S., Kuroda, Y., Kodera, K., and Watanabe, S.: Robust enhancement of tropical convective activity by the 2019 Antarctic sudden stratospheric warming, Geophys. Res. Lett., 47, e2020GL088 743, https://doi.org/10.1029/2020GL088743, 2020.

Oberheide, J., Forbes, J., Häusler, K., Wu, Q., and Bruinsma, S.: Tropospheric tides from 80 to 400 km: Propagation, interannual variability, and solar cycle effects, J. Geophys. Res.: Atmospheres, 114, https://doi.org/10.1029/2009JD012388, 2009.

Oberheide, J., Forbes, J., Zhang, X., and Bruinsma, S.: Climatology of upward propagating diurnal and semidiurnal tides in the thermosphere, J. Geophys. Res.: Space Physics, 116, https://doi.org/10.1029/2011JA016784, 2011.

Palo, S., Forbes, J., Zhang, X., Russell Iii, J., and Mlynczak, M.: An eastward propagating two-day wave: Evidence for nonlinear planetary wave and tidal coupling in the mesosphere and lower thermosphere, Geophys. Res. Lett., 34, https://doi.org/10.1029/2006GL027728, 2007.

Pancheva, D. and Mukhtarov, P.: Strong evidence for the tidal control on the longitudinal structure of the ionospheric F-region, Geophys. Res. Lett., 37, https://doi.org/10.1029/2010GL044039, 2010.

Pancheva, D., Mukhtarov, P., and Siskind, D. E.: The quasi-6-day waves in NOGAPS-ALPHA forecast model and their climatology in MLS/Aura measurements (2005–2014), J. Atmos. Sol.-Terr. Phys., 181, 19–37, https://doi.org/10.1016/j.jastp.2018.10.008, 2018.

Pedatella, N., Liu, H.-L., and Hagan, M.: Day-to-day migrating and nonmigrating tidal variability due to the six-day planetary wave, J. Geophys. Res.: Space Physics, 117, https://doi.org/10.1029/2012JA017581, 2012a.

Pedatella, N., Liu, H.-L., Richmond, A., Maute, A., and Fang, T.-W.: Simulations of solar and lunar tidal variability in the mesosphere and lower thermosphere during sudden stratosphere warmings and their influence on the low-latitude ionosphere, J. Geophys. Res.: Space Physics, 117, https://doi.org/10.1029/2012JA017792, 2012b.

Pedatella, N., Liu, H.-L., Sassi, F., Lei, J., Chau, J., and Zhang, X.: Ionosphere variability during the 2009 SSW: Influence of the lunar semidiurnal tide and mechanisms producing electron density variability, J. Geophys. Res.: Space Physics, 119, 3828–3843, https://doi.org/10.1002/2014JA019849, 2014.

Pedatella, N., Chau, J., Schmidt, H., Goncharenko, L., Stolle, C., Hocke, K., Harvey, V., Funke, B., and Siddiqui, T.: How Sudden stratospheric warmings affect the whole atmosphere, EOS, https://doi.org/10.1029/2018EO092441, 2018.

Pfister, L.: Baroclinic instability of easterly jets with applications to the summer mesosphere, Journal of Atmospheric Sciences, 42, 313–330, 1985.

575   Pogoreltsev, A., Fedulina, I., Mitchell, N., Muller, H., Luo, Y., Meek, C., and Manson, A.: Global free oscillations of the atmosphere and secondary planetary waves in the mesosphere and lower thermosphere region during August/September time conditions, J. Geophys. Res.: Atmospheres, 107, ACL–24, https://doi.org/10.1029/2001JD001535, 2002.

Qin, Y., Gu, S.-Y., and Dou, X.: A New Mechanism for the Generation of Quasi-6-Day and Quasi-10-Day Waves During the 2019 Antarctic Sudden Stratospheric Warming, J. Geophys. Res.: Atmospheres, 126, e2021JD035 568, https://doi.org/10.1029/2021JD035568, 2021a.

580   Qin, Y., Gu, S.-Y., Teng, C.-K.-M., Dou, X.-K., Yu, Y., and Li, N.: Comprehensive study of the climatology of the quasi-6-day wave in the MLT region based on Aura/MLS observations and SD-WACCM-X simulations, J. Geophys. Res.: Space Physics, 126, e2020JA028 454, https://doi.org/10.1029/2020JA028454, 2021b.

Qin, Y., Gu, S.-Y., Dou, X., Teng, C.-K.-M., Yang, Z., and Sun, R.: Southern Hemisphere Response to the Secondary Planetary Waves Generated During the Arctic Sudden Stratospheric Final Warmings: Influence of the Quasi-Biennial Oscillation, J. Geophys. Res.: Atmospheres,
585   p. e2022JD037730, https://doi.org/10.1029/2022JD037730, 2022.

Rao, J., Garfinkel, C. I., White, I. P., and Schwartz, C.: The Southern Hemisphere minor sudden stratospheric warming in September 2019 and its predictions in S2S models, J. Geophys. Res.: Atmospheres, 125, e2020JD032 723, https://doi.org/10.1029/2020JD032723, 2020.

Safieddine, S., Bouillon, M., Paracho, A.-c., Jumelet, J., Tence, F., Pazmino, A., Goutail, F., Wespes, C., Bekki, S., Boynard, A., et al.: Antarctic ozone enhancement during the 2019 sudden stratospheric warming event, Geophys. Res. Lett., 47, e2020GL087 810,
590   https://doi.org/10.1029/2020GL087810, 2020.

Salby, M. L.: The 2-day wave in the middle atmosphere: Observations and theory, J. Geophys. Res.: Oceans, 86, 9654–9660, https://doi.org/10.1029/JC086iC10p09654, 1981a.

Salby, M. L.: Rossby normal modes in nonuniform background configurations. Part I: Simple fields, J. Atmos. Sci., 38, 1803–1826, https://doi.org/10.1175/1520-0469(1981)038<1803:RNMINB>2.0.CO;2, 1981b.

595   Salby, M. L.: Rossby normal modes in nonuniform background configurations. Part II. Equinox and solstice conditions, J. Atmos. Sci., 38, 1827–1840, https://doi.org/10.1175/1520-0469(1981)038<1827:RNMINB>2.0.CO;2, 1981c.

Salby, M. L.: Survey of planetary-scale traveling waves: The state of theory and observations, Rev. Geophys., 22, 209–236, https://doi.org/10.1029/RG022i002p00209, 1984.

Salby, M. L. and Callaghan, P. F.: Seasonal amplification of the 2-day wave: Relationship between normal mode and instability, J. Atmos.
600   Sci., 58, 1858–1869, https://doi.org/10.1175/1520-0469(2001)058<1858:SAOTDW>2.0.CO;2, 2001.

Sassi, F., Garcia, R., and Hoppel, K.: Large-scale Rossby normal modes during some recent Northern Hemisphere winters, J. Atmos. Sci., 69, 820–839, https://doi.org/10.1175/JAS-D-11-0103.1, 2012.

Sassi, F., Liu, H.-L., Ma, J., and Garcia, R. R.: The lower thermosphere during the Northern Hemisphere winter of 2009: A modeling study using high-altitude data assimilation products in WACCM-X, J. Geophys. Res.: Atmospheres, 118, 8954–8968,
605   https://doi.org/10.1002/jgrd.50632, 2013.

Sassi, F., Liu, H.-L., and Emmert, J. T.: Traveling planetary-scale waves in the lower thermosphere: Effects on neutral density and composition during solar minimum conditions, J. Geophys. Res.: Space Physics, 121, 1780–1801, https://doi.org/10.1002/2015JA022082, 2016.

Schunk, R. and Sojka, J. J.: Ionosphere-thermosphere space weather issues, J. Atmos. Terr. Phys., 58, 1527–1574, https://doi.org/10.1016/0021-9169(96)00029-3, 1996.

610   Siddiqui, T., Maute, A., and Pedatella, N.: On the importance of interactive ozone chemistry in Earth-system models for studying mesosphere-lower thermosphere tidal changes during sudden stratospheric warmings, J. Geophys. Res.: Space Physics, 124, 10 690–10 707, https://doi.org/10.1029/2019JA027193, 2019.

Siddiqui, T., Yamazaki, Y., Stolle, C., Maute, A., Laštovička, J., Edemskiy, I., Mošna, Z., and Sivakandan, M.: Understanding the to-tal electron content variability over Europe during 2009 and 2019 SSWs, J. Geophys. Res.: Space Physics, 126, e2020JA028 751, https://doi.org/10.1029/2020JA028751, 2021.

Siddiqui, T. A., Maute, A., Pedatella, N., Yamazaki, Y., Lühr, H., and Stolle, C.: On the variability of the semidiurnal solar and lunar tides of the equatorial electrojet during sudden stratospheric warmings, in: Annales Geophysicae, vol. 36, pp. 1545–1562, Copernicus GmbH, 2018.

Siddiqui, T. A., Chau, J. L., Stolle, C., and Yamazaki, Y.: Migrating solar diurnal tidal variability during Northern and Southern Hemisphere Sudden Stratospheric Warmings, Earth, Planets and Space, 74, 1–17, https://doi.org/10.1186/s40623-022-01661-y, 2022.

Sobhkhiz-Miandehi, S., Yamazaki, Y., Arras, C., Miyoshi, Y., and Shinagawa, H.: Comparison of the tidal signatures in sporadic E and vertical ion convergence rate, using FORMOSAT-3/COSMIC radio occultation observations and GAIA model, Earth, Planets and Space, 74, 1–13, https://doi.org/10.1186/s40623-022-01637-y, 2022.

Stober, G., Baumgarten, K., McCormack, J. P., Brown, P., and Czarnecki, J.: Comparative study between ground-based observations and NAVGEM-HA analysis data in the mesosphere and lower thermosphere region, Atmospheric chemistry and physics, 20, 11 979–12 010, 2020.

Torrence, C. and Compo, G. P.: A practical guide to wavelet analysis, Bull. Am. Meteorol., 79, 61–78, https://doi.org/10.1175/1520-0477(1998)079<0061:APGTWA>2.0.CO;2, 1998.

Wang, H., Akmaev, R., Fang, T.-W., Fuller-Rowell, T., Wu, F., Maruyama, N., and Iredell, M.: First forecast of a sudden strato-spheric warming with a coupled whole-atmosphere/ionosphere model IDEA, J. Geophys. Res.: Space Physics, 119, 2079–2089, https://doi.org/10.1002/2013JA019481, 2014.

Wang, J. C., Palo, S. E., Forbes, J., Marino, J., Moffat-Griffin, T., and Mitchell, N.: Unusual quasi 10-day planetary wave activity and the ionospheric response during the 2019 Southern Hemisphere sudden stratospheric warming, J. Geophys. Res.: Space Physics, 126, e2021JA029 286, https://doi.org/10.1029/2021JA029286, 2021a.

Wang, J. C., Palo, S. E., Liu, H.-L., and Siskind, D.: Day-to-Day Variability of Diurnal Tide in the Mesosphere and Lower Thermosphere Driven From Below, J. Geophys. Res.: Space Physics, 126, e2019JA027 759, https://doi.org/10.1029/2019JA027759, 2021b.

Wargan, K., Weir, B., Manney, G. L., Cohn, S. E., and Livesey, N. J.: The anomalous 2019 Antarctic ozone hole in the GEOS Constituent Data Assimilation System with MLS observations, J. Geophys. Res.: Atmospheres, 125, e2020JD033 335, https://doi.org/10.1029/2020JD033335, 2020.

Wells, D. E., Vaníček, P., and Pagiatakis, S. D.: Least squares spectral analysis revisited, Tech. rep., Department of Surveying Engineering, University of New Brunswick Fredericton, N.B., Canada, https://gge.ext.unb.ca/Pubs/TR84.pdf, 1985.

Wheeler, M. and Kiladis, G. N.: Convectively coupled equatorial waves: Analysis of clouds and temperature in the wavenumber–frequency domain, J. Atmos. Sci., 56, 374–399, https://doi.org/10.1175/1520-0469(1999)056<0374:CCEWAO>2.0.CO;2, 1999.

Wu, D., Hays, P., Skinner, W., Marshall, A., Burrage, M., Lieberman, R., and Ortland, D.: Observations of the quasi 2-day wave from the High Resolution Doppler Imager on UARS, Geophys. Res. Lett., 20, 2853–2856, https://doi.org/10.1029/93GL03008, 1993.

Wu, D., Hays, P., and Skinner, W.: Observations of the 5-day wave in the mesosphere and lower thermosphere, Geophys. Res. Lett., 21, 2733–2736, https://doi.org/10.1016/j.jastp.2005.05.010, 1994.

Yamazaki, Y.: Quasi-6-day wave effects on the equatorial ionization anomaly over a solar cycle, J. Geophys. Res.: Space Physics, 123, 9881–9892, https://doi.org/10.1029/2018JA026014, 2018.

Yamazaki, Y. and Matthias, V.: Large-amplitude quasi-10-day waves in the middle atmosphere during final warmings, J. Geophys. Res.: Atmospheres, 124, 9874–9892, https://doi.org/10.1029/2019JD030634, 2019.

Yamazaki, Y., Matthias, V., Miyoshi, Y., Stolle, C., Siddiqui, T., Kervalishvili, G., Laštovička, J., Kozubek, M., Ward, W., Themens, D. R., et al.: September 2019 Antarctic sudden stratospheric warming: Quasi-6-day wave burst and ionospheric effects, Geophys. Res. Lett., 47, e2019GL086 577, https://doi.org/10.1029/2019GL086577, 2020a.

Yamazaki, Y., Miyoshi, Y., Xiong, C., Stolle, C., Soares, G., and Yoshikawa, A.: Whole atmosphere model simulations of ultrafast Kelvin wave effects in the ionosphere and thermosphere, J. Geophys. Res.: Space Physics, 125, e2020JA027 939, https://doi.org/10.1029/2020JA027939, 2020b.

Yamazaki, Y., Matthias, V., and Miyoshi, Y.: Quasi-4-Day Wave: Atmospheric Manifestation of the First Symmetric Rossby Normal Mode of Zonal Wavenumber 2, J. Geophys. Res.: Atmospheres, 126, e2021JD034 855, https://doi.org/10.1029/2021JD034855, 2021.

Yamazaki, Y., Harding, B. J., Qiu, L., Stolle, C., Siddiqui, T., Miyoshi, Y., Englert, C. R., and England, S.: Monthly climatologies of zonal-mean and tidal winds in the thermosphere as observed by ICON/MIGHTI during April 2020–March 2022, Earth and Space Science, 10, e2023EA002 962, https://doi.org/10.1029/2023EA002962, 2023.

Yano, J.-I., Moncrieff, M. W., Wu, X., and Yamada, M.: Wavelet analysis of simulated tropical convective cloud systems. Part I: Basic analysis, Journal of the atmospheric sciences, 58, 850–867, 2001.

Yano, J.-I., Bechtold, P., Redelsperger, J.-L., and Guichard, F.: Wavelet-compressed representation of deep moist convection, Monthly weather review, 132, 1472–1486, 2004.

Yiğit, E. and Medvedev, A. S.: Internal wave coupling processes in Earth's atmosphere, Adv. Space Res., 55, 983–1003, https://doi.org/10.1016/j.asr.2014.11.020, 2015.

Yin, S., Ma, Z., Gong, Y., Zhang, S., and Li, G.: Response of quasi-10-day waves in the MLT region to the sudden stratospheric warming in March 2020, Adv. Space Res., https://doi.org/doi.org/10.1016/j.asr.2022.10.054, 2022.

Yu, F. R., Huang, K. M., Zhang, S. D., Huang, C. M., Yi, F., Gong, Y., Wang, R., Li, G., and Ning, B.: Quasi 10-and 16-day wave activities observed through meteor radar and MST radar during stratospheric final warming in 2015 spring, J. Geophys. Res.: Atmospheres, 124, 6040–6056, https://doi.org/10.1029/2019JD030630, 2019.

Yue, J., Liu, H.-L., and Chang, L. C.: Numerical investigation of the quasi 2 day wave in the mesosphere and lower thermosphere, J. Geophys. Res.: Atmospheres, 117, https://doi.org/10.1029/2011JD016574, 2012.

Yue, X., Schreiner, W. S., Lei, J., Rocken, C., Hunt, D. C., Kuo, Y.-H., and Wan, W.: Global ionospheric response observed by COSMIC satellites during the January 2009 stratospheric sudden warming event, J. Geophys. Res.: Space Physics, 115, https://doi.org/10.1029/2010JA015466, 2010.

Zhang, X., Forbes, J. M., Hagan, M. E., Russell III, J. M., Palo, S. E., Mertens, C. J., and Mlynczak, M. G.: Monthly tidal temperatures 20–120 km from TIMED/SABER, J. Geophys. Res.: Space Physics, 111, https://doi.org/10.1029/2005JA011504, 2006.

Zhao, Y., Taylor, M. J., Pautet, P.-D., Moffat-Griffin, T., Hervig, M. E., Murphy, D. J., French, W., Liu, H.-L., Pendleton Jr, W. R., and Russell III, J.: Investigating an unusually large 28-day oscillation in mesospheric temperature over Antarctica using ground-based and satellite measurements, J. Geophys. Res.: Atmospheres, 124, 8576–8593, https://doi.org/10.1029/2019JD030286, 2019.
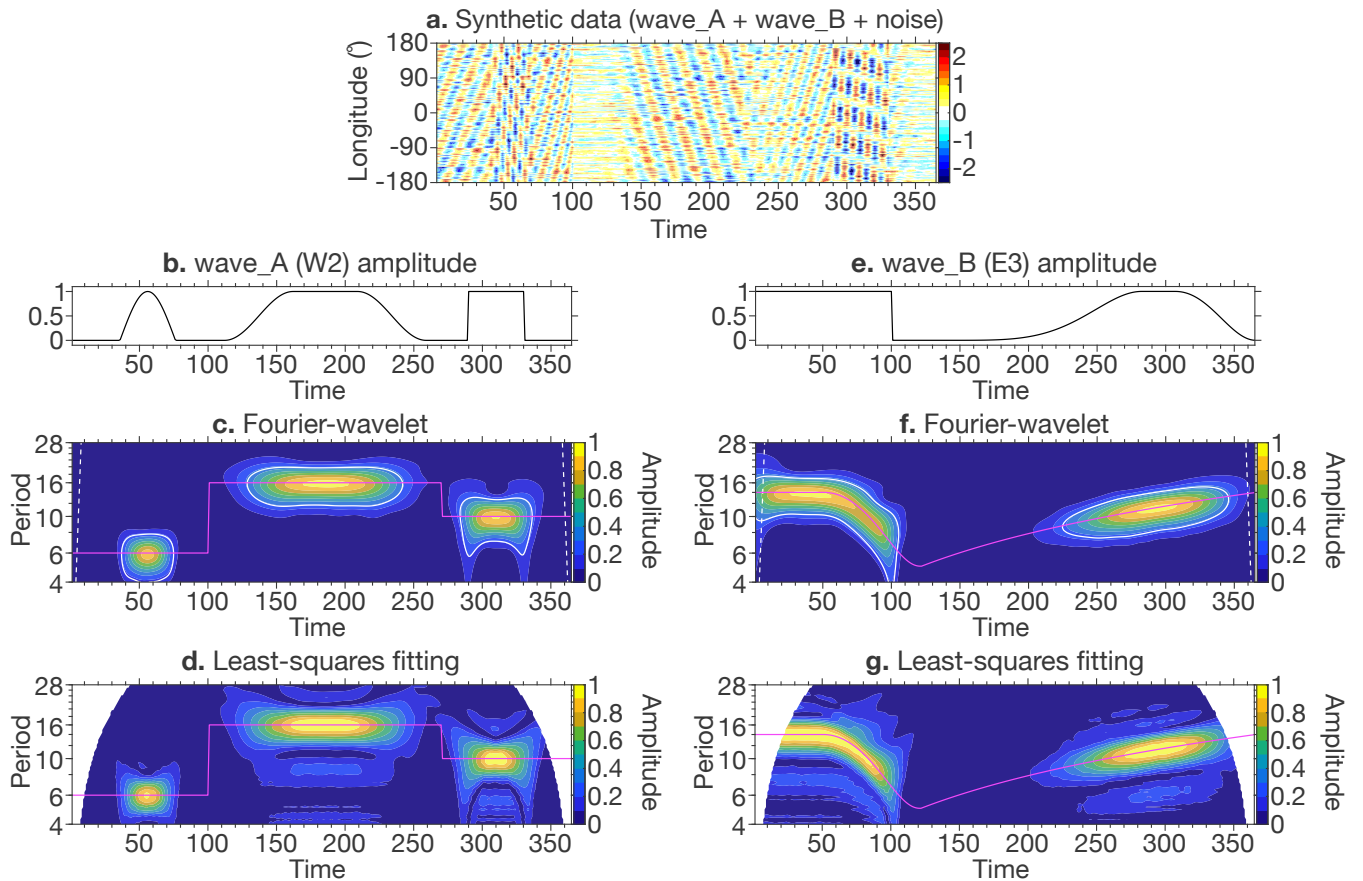
Figure 1. (a) Synthetic data containing wave_A (westward-propagating with zonal wavenumber 2, W2) and wave_B (eastward-propagating with zonal wavenumber 3, E3), along with noise. (b) Amplitude of wave_A. (c) Phase of wave_A (magenta line), and Fourier-wavelet amplitude spectrum for W2 (contour plot). The white curves indicate the 95% confidence level, while the white dashed lines show the cone of influence. (d) Same as (c) except that the amplitude spectrum is derived with the least-squares fitting method. (e–g) Same as (b–d) but for wave_B. The amplitude spectra are for E3.

GAIA

a. T (90°S) & $\overline{U}$ (60°S) at 10 hPa

b. Zonal wind (equator, 100 km)

c. Fourier-wavelet (W1, equator, 100 km)

d. Fourier-wavelet (E1, equator, 100 km)

e. Fourier-wavelet (W2, equator, 100 km)

f. Fourier-wavelet (E2, equator, 100 km)

g. Fourier-wavelet (W3, equator, 100 km)

h. Fourier-wavelet (E3, equator, 100 km)
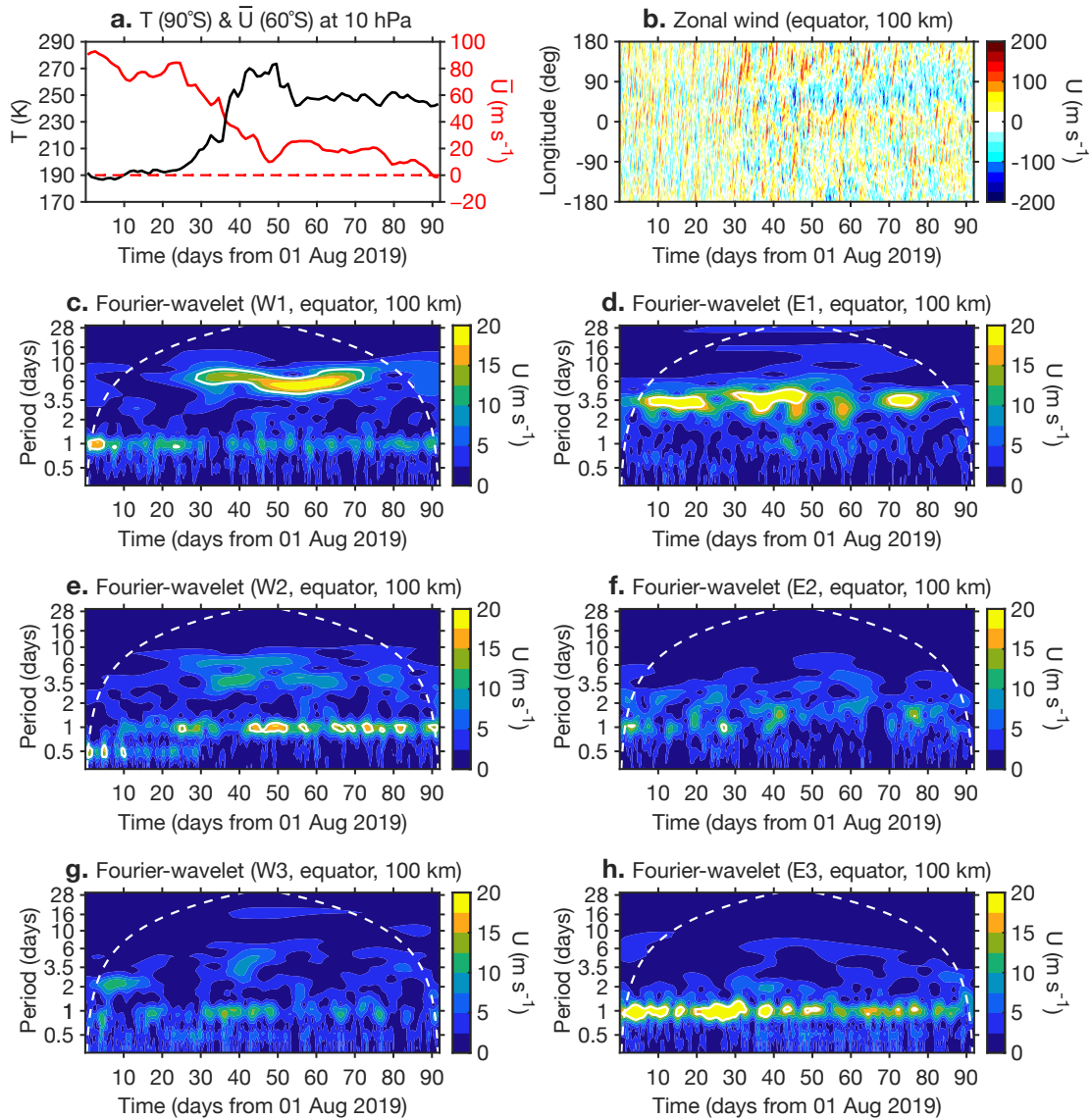
Figure 2. GAIA model simulation for the period August–October 2019. (a) Polar temperature and zonal mean zonal wind velocity at 60°N at 10 hPa. (b) Zonal wind velocity over the equator at a height of 100 km. (c–h) Fourier-wavelet spectra of the equatorial zonal wind velocity at 100 km for (c) the westward-propagating zonal wavenumber 1 (W1) component, (d) the eastward-propagating zonal wavenumber 1 (E1) component, (e) the westward-propagating zonal wavenumber 2 (W2) component, (f) the eastward-propagating zonal wavenumber 2 (E2) component, (g) the westward-propagating zonal wavenumber 3 (W3) component and (h) the eastward-propagating zonal wavenumber 3 (E3) component. The white curves indicate the 95% confidence level, while the white dashed lines show the cone of influence.
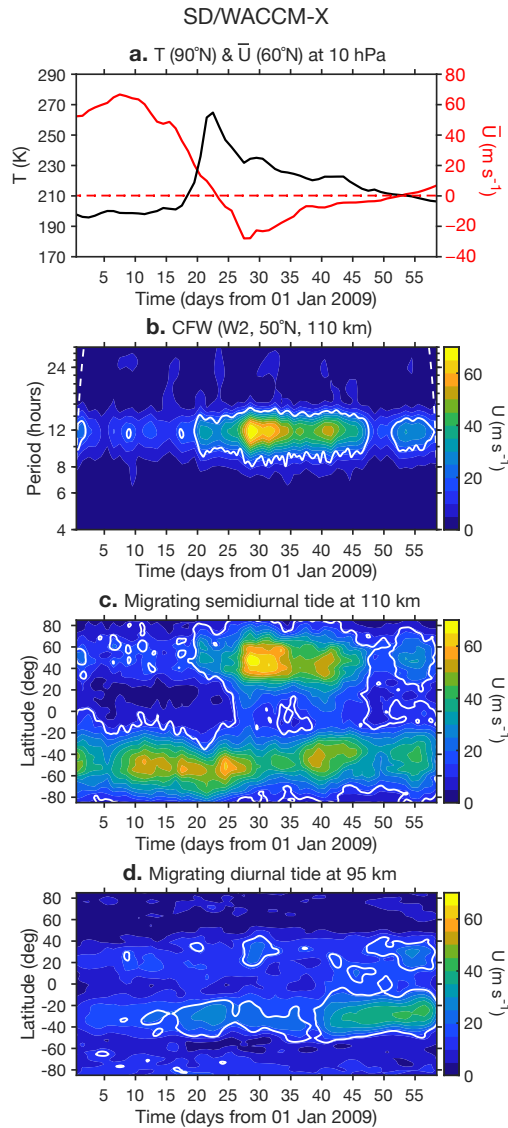
Figure 3. SD/WACCM-X model simulation for the period January–February 2009. (a) Polar temperature and zonal mean zonal wind velocity at 60°N at 10 hPa. (b) Fourier-wavelet spectrum of the zonal wind velocity at 50°N and 110 km. The white curves indicate the 95% confidence level, while the white dashed lines show the cone of influence. (c) Amplitude of the migrating semidiurnal tide in the zonal wind velocity at 110 km as determined by the Fourier-wavelet technique. (d) Amplitude of the migrating diurnal tide in the zonal wind velocity at 95 km as determined by the Fourier-wavelet technique.
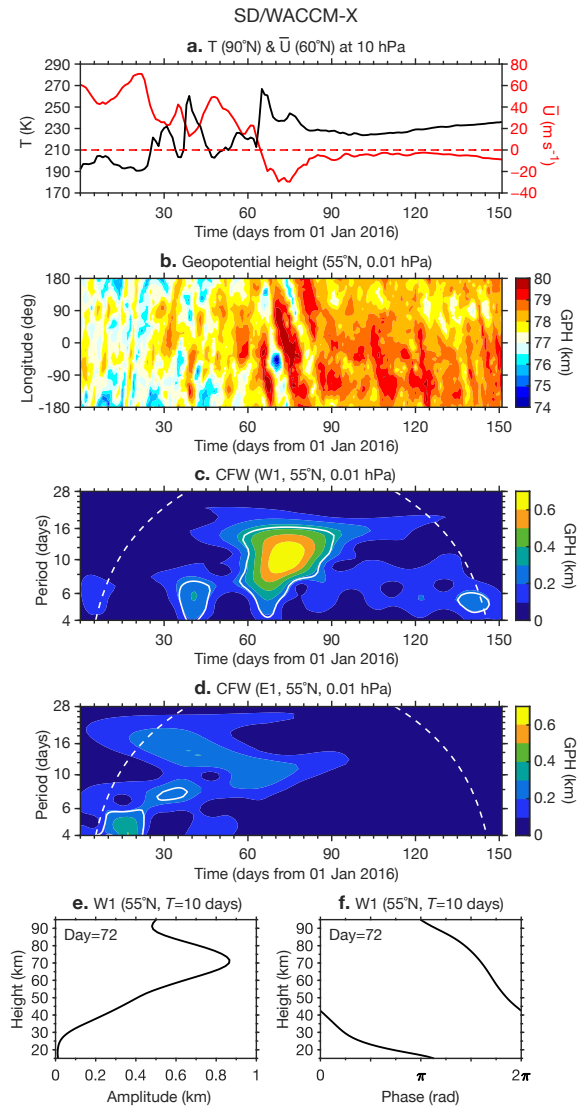
Figure 4. SD/WACCM-X model simulation for the period January–May 2016. (a) Polar temperature and zonal mean zonal wind velocity at 60°N at 10 hPa. (b) Geopotential height at 55°N at 0.01 hPa. (c–d) Fourier-wavelet spectra of the geopotential height at 55°N at 0.01 hPa for (c) the westward-propagating zonal wavenumber 1 (W1) component and (d) the eastward-propagating zonal wavenumber 1 (E1) component. (e–f) Height profiles of (e) amplitude and (f) phase of the W1 component at a period of 10 days at 55°N and 0.01 hPa on Day 72 as determined by the Fourier-wavelet technique.